AIMS Materials Science, 12(2): 258–277.
DOI: 10.3934/matersci.2025014
Received: 05 January 2025
Revised: 13 March 2025
Accepted: 24 March 2025
Published: 31 March 2025

http://www.aimspress.com/journal/Materials

*Research article*

# Molecular structure and thermal conductivity of hydrated sodium aluminosilicate (N-A-S-H) gel under different Si/Al ratios and temperatures: A molecular dynamics analysis

**Yun-Lin Liu[1], Si-Yu Ren[1], Dong-Hua Wang[1], Ding-Wei Yang[1], Ming-Feng Kai[2] and Dong Guo[3,*]**

[1] College of Civil Engineering, Anhui Jianzhu University, Hefei 230601, China
[2] School of Mechanics and Construction Engineering, Jinan University, Guangdong 510632, China
[3] School of Civil Engineering and Transportation, Guangzhou University, Guangdong 510006, China

* **Correspondence:** Email: dong.ce.guo@connect.polyu.hk.

**Abstract:** Geopolymer materials have emerged as promising alternatives to ordinary Portland cementitious materials, offering more sustainable solutions for concrete production. Sodium aluminosilicate hydrate (N-A-S-H) serves as a crucial component in geopolymer concrete, while its thermomechanical properties at elevated temperatures remain relatively underexplored. This study examined the molecular structural variations of N-A-S-H within a temperature range of 300–900 K. The influence of different Si/Al ratios and temperature levels on molecular characteristics and atomic mobility was analyzed using the radial distribution function (RDF) and mean square displacement (MSD). The thermal conductivity of the N-A-S-H gel was determined using the Müller-Plathe reverse nonequilibrium molecular dynamics (RNEMD) method. Results show that as temperature increases, the mobility of Si and Al atoms is enhanced, and the thermal conductivity of N-A-S-H gel ranges from 1.431 to 1.857 W/m/K. The thermal conductivity increases with higher Si/Al ratios and elevated temperatures, suggesting decreased thermal insulation performance at higher Si/Al ratios and temperatures.

**Keywords:** molecular dynamics (MD) modeling; N-A-S-H; thermal properties; thermal conductivity; Si/Al ratio

## 1. Introduction

Concrete is the most widely used construction material, with annual consumption exceeding 10 billion tons and continuing to rise [1]. Ordinary Portland cement (OPC), the primary binder, is produced through high-temperature calcination of limestone, a process that is energy-intensive and responsible for approximately 5% of global $CO_2$ emissions [2–5]. Geopolymers have emerged as a promising alternative, offering lower carbon emissions and the potential to utilize industrial waste by-products [6,7]. Composed mainly of silicon and aluminum-rich industrial waste like fly ash and ground granulated blast furnace slag, geopolymers undergo chemical reactions with alkaline activators, resulting in a solid material with excellent mechanical properties and durability [8–11]. They also exhibit desirable characteristics such as rapid setting times, high strength, low thermal conductivity, and good thermal stability [12–14].

Recent research has demonstrated that geopolymers exhibit excellent thermal stability and insulation performance at elevated temperatures [15], making them increasingly suitable for application in fire insulation materials in construction [16,17]. Cheng et al. [16] investigated the thermal insulation behavior of a 10 mm thick geopolymer panel, with granular blast furnace slag as the precursor. After exposure to flames at 1100 °C for 35 min, the temperature on the backfire surface remained below 350 °C. Temuujin et al. [18] studied the fire resistance of geopolymer coatings made from fly ash and found that coatings with thicknesses of 0.6 and 1.5 mm exhibited a temperature lag of approximately 7 and 9 min, respectively, before the covered structural surface reached the exposed fire temperature. Coatings with 20 mm thickness were expected to maintain a thermal delay of over 100 min.

The fire-resistant insulation performance of geopolymer materials is primarily determined by their thermal stability and heat insulation properties. The material must retain its structural integrity at elevated temperatures, preventing degradation or failure during exposure to heat or fire. Moreover, its thermal conductivity should be sufficiently low to minimize heat transfer from the external environment to the protected surface. As reported by Qomi et al. [19], the thermal conductivity of calcium silicate hydrates (C-S-H) is in the range of 0.74–1.25 W/m/K. While sodium aluminosilicate hydrate (N-A-S-H) exhibited higher thermal conductivity, ranging from 1.665 to 1.916 W/m/K [20]. In addition, the thermal stability of geopolymers depends on their chemical composition, which can be optimized by adjusting the Si/Al ratio [21] and water content [18]. This stability can be further enhanced by incorporating steel fibers and waste iron powder [22,23]. Furthermore, the thermal conductivity of geopolymers can be modified by adding heat-insulating fillers [24], and it is also influenced by materials' service temperatures [23].

Geopolymers are inorganic polymers with an amorphous microstructure, and N-A-S-H is their primary component. The performance of geopolymers is directly influenced by the properties of N-A-S-H gel. The microstructure of N-A-S-H is influenced by several factors, including the Si/Al ratio [25], temperature exposure [26], curing conditions [27], and water-to-binder ratio [28]. Although numerous macro-level experiments have investigated the high-temperature performance of geopolymer materials, there is a lack of in-depth understanding of the molecular structural changes and performance variations of N-A-S-H, a key component of geopolymers [29–32]. The thermal conductivity should be attributed to the thermal motion of molecules and atoms, which is difficult to analyze accurately at the macroscopic scale. To address this gap, molecular dynamics (MD) simulations offer a powerful tool for investigating the molecular-level behavior of N-A-S-H gel. This

method allows for the detailed exploration of structural changes and interactions at the atomic scale, providing valuable insights into the thermal performance and other properties of geopolymers that are difficult to observe through traditional experimental approaches.

Numerous studies have indicated that molecular dynamics simulations can efficiently and accurately predict the thermal properties of materials, effectively compensating for measurement errors caused by external environmental factors during experimental processes [33–36]. Based on MD simulations, the structures of geopolymers at temperatures ranging from 273 to 4273 K and Si/Al ratios ranging from 1:1 to 3:1 were compared by Kupwade-Patil et al. [25] They found that N-A-S-H geopolymer structures were more stable at elevated temperatures compared to their potassium aluminosilicate gel (K-A-S-H) counterparts. Additionally, a Si/Al ratio of 2:1 contributed to a superior thermal stability of N-A-S-H, which can be attributed to the increased energy required to break the molecular bonds at shortened bond lengths in temperatures from 298 to 4273 K. Liu et al. [20] investigated the effects of varying Si/Al ratios, porosity, and water content on the thermal conductivity of geopolymers. They found that the thermal conductivity of N-A-S-H increased by 15.1% when the Si/Al ratio was raised from 1 to 3.

MD simulations of thermal conductivity can be categorized into equilibrium molecular dynamics (EMD) and nonequilibrium molecular dynamics (NEMD) [37–39]. EMD and NEMD are based on the fluctuation-dissipation theorem and Fourier's law of conduction, respectively, with NEMD being more representative of experimental conditions. Additionally, EMD is typically more computationally intensive, and its results are more sensitive to the choice of simulation parameters [40]. Both NEMD and EMD methods are subject to finite-size effects, but these effects are more pronounced in NEMD due to the presence of interfaces at the heat source and sink. This effect arises from the relationship between the system size and the phonon mean free path. When the system size is smaller than or comparable to the phonon-free path, it can lead to inaccuracies in thermal conductivity calculations. Furthermore, in the NEMD method, a temperature gradient must be applied, which may introduce nonlinear effects, and the results are typically limited to thermal conductivity in one single direction. In contrast, EMD simulations provide a more comprehensive assessment of thermal conductivity in all directions [20,41].

The introduction of the reverse nonequilibrium molecular dynamics (RNEMD) method by Müller-Plathe has addressed several challenges in thermal conductivity simulations [42]. This method directly applies a heat flux and measures the resulting temperature gradient, avoiding the large fluctuations in heat flux that can occur in the traditional method. As a result, RNEMD offers faster and more stable convergence. Furthermore, RNEMD does not require complex boundary conditions and can conserve total linear momentum, total kinetic energy, or total energy, while eliminating the need for thermostats to regulate temperature. This makes RNEMD applicable to a wider range of simulation systems. Compared to traditional NEMD modeling, RNEMD provides a more accurate approach for studying changes in thermal conductivity across different temperature ranges, considering various influencing factors, and enabling faster data collection and analysis [42,43] The RNEMD method has been widely used to calculate the thermal conductivity of various materials, including nanofluid [44], boron nitride/epoxy resin composites [45], graphene nanoribbons [46], and Fe-Cr alloys [47].

Based on the above, geopolymers are promising high-temperature insulation materials, with their primary properties linked to the molecular structure of N-A-S-H and dependent on the Si/Al ratio. Most existing research has focused on experimental studies at the macroscale, leaving a gap in investigations into how the N-A-S-H molecular structure and thermal conductivity vary with temperature.

Thermodynamic MD simulations are capable of efficiently and accurately predicting the thermal properties of materials, as well as analyzing variations in bond lengths, molecular structures, and thermal conductivity at extreme temperatures. These simulations are expected to provide valuable insights into the thermodynamic characteristics of N-A-S-H geopolymer gels. Expanding research in this area will deepen our understanding of their thermal behavior at the molecular level, ultimately contributing to the development of geopolymers with enhanced performance for high-temperature applications.

## 2. Materials and methods

### *2.1. Construction of molecular structure*

N-A-S-H is primarily composed of a random three-dimensional tetrahedral lattice containing silicon and aluminum units, water, and free metal cations [48]. The molecular structure of $Na_2Si_2O_5$ glass closely resembles the composition system of geopolymers [49,50]. Therefore, in this study, the molecular structure of $Na_2Si_2O_5$ glass was chosen as the initial structure for constructing the molecular model of the geopolymer [51].

To study the effects of the Si/Al ratio and temperature on the structure and thermal conductivity of geopolymers, three models with varying Si/Al ratios were constructed. The molecular models with different Si/Al ratios were obtained by randomly substituting Si atoms with Al atoms. Since Si in these structures formed four coordinated bonds, substituting Si with Al atoms created a charge imbalance. To maintain charge balance, $Na^+$ ions were redistributed, matching the number of Al atoms. Geopolymers typically exhibit an amorphous structure. Therefore, the model was created using the Amorphous Cell module. Water molecules, distributed at a specific ratio, were randomly inserted into the cavities of the geopolymer gel to form the N-A-S-H molecular model.

Energy optimization is a critical step in molecular dynamics to ensure the stability of the model. In this study, energy optimization was performed using three different algorithms (steepest descent, conjugate gradient, and Newton–Raphson method) to achieve the minimum energy state. After optimization, periodic boundary conditions were applied in the X, Y, and Z directions to simplify the simulation.

Molecular dynamics simulations are typically divided into two stages: model equilibration and data collection. In the model equilibration stage, the system was first heated to 2500 K and equilibrated for 100 ps under the isobaric-isothermal (NPT) ensemble. Following this, a quenching simulation was performed under the NPT ensemble, where the system was heated to 2500 K and then gradually cooled to 300 K, followed by equilibration at 300 K for 100 ps. Afterward, the system was run for an additional 100 ps at 300 K and 1 atm pressure under the NPT ensemble, with a time step of 1 fs. Once the equilibration stage was complete, the system transitioned to the data collection stage. During this stage, the system was further equilibrated using the canonical ensemble (NVT) at 300 K, with a time step of 1 fs for 100 ps.

The final amorphous geopolymer structure model is shown in Figure 1, where white balls represent hydrogen atoms, red balls represent oxygen atoms, pink balls represent aluminum atoms, yellow balls represent silicon atoms, and purple balls represent sodium atoms. The molecular model composition is summarized in Table 1.

**Table 1.** Composition of the simulated geopolymer.

| Si/Al | Na/Al | $H_2O$/Al | Number of atoms |
|---|---|---|---|
| 1 | 1 | 1 | 701 |
| 2 | 1 | 1 | 611 |
| 3 | 1 | 1 | 571 |

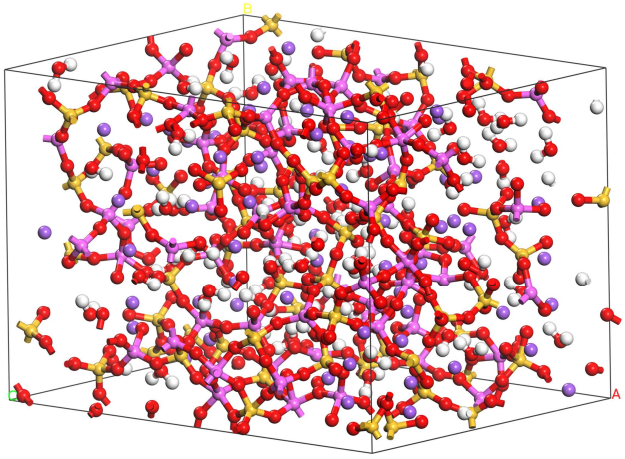

**Figure 1.** N-A-S-H model with Si/Al = 1.

### *2.2. Force field and potential functions*

The forcefield is used to calculate interatomic forces in MD simulation. It is an empirical fitting expression describing the system's potential energy *U*, which is an algebraic function Eq 1:

$$U = U_{valance} + U_{non-bond} \quad (1)$$

Here, *U* represents potential energy, $U_{valance}$ refers to the bond energy, and $U_{non-bond}$ represents the non-bond energy. The bond energy can be further divided into bond diagonal terms (representing bond stretching) and bond cross terms (representing bond-angle interactions). The non-bonded energies include van der Waals forces, electrostatic interactions, and hydrogen bonding.

There are various types of force fields, and no single universal force field can accurately represent all systems. It is important to select a force field that aligns with the specific requirements of the model to ensure simulations and reliable analysis. Non-reactive forcefields such as COMPASS II [52], Dreiding [53], and Universal [54] are commonly used for the molecular dynamics simulation of N-A-S-H gel. COMPASS II is an advanced, well-established forcefield designed for atomic simulations. It is a valence force field, meaning all bonds are treated as valence, and metal bonds, especially ions, are present. Silicon bonds are covalent, and metal cations (e.g., $Na^+$) are considered free and typically located near Al atoms. However, COMPASS II is not ideal for N-A-S-H gel simulations due to the presence of free ions and covalent bonding.

It is worth noting that in recent years, ReaxFF and Universal Force Field (UFF) have also been applied to study the molecular behavior of N-A-S-H [54,55]. ReaxFF offers advantages in dealing with reactivity and bond breaking, while UFF is an all-element force field that accurately represents most

elements of the periodic table, offering a more comprehensive view of the system. Therefore, we have chosen the UFF in this study as it provides a better description of the variations in the non-reactive system [54]. UFF is a harmonic force field, where bond stretching is described by the harmonic term, the angle bending by a three-term Fourier cosine expansion, and torsions and inversions by cosine-Fourier expansion terms. Non-bonded interactions are modeled using the Lennard-Jones potential for van der Waals interactions and a distance-dependent Coulombic term for electrostatic interactions. The potential energy equation for the universal force field is Eq 2:

$$E = E_R + E_\theta + E_\phi + E_\omega + E_{vdw} + E_{el} \tag{2}$$

In this equation, the bond energy includes contributions from bond stretching ($E_R$), bond angle bending ($E_\theta$), dihedral angle torsion ($E_\phi$), and inversion energy ($E_\omega$). The non-bonded interactions consist of van der Waals forces ($E_{vdw}$) and electrostatic interactions ($E_{el}$).

### *2.3. Thermal conductivity calculation method*

In the RNEMD method, the energy $\nabla E$ is variable, and energy exchange occurs through the transfer of kinetic energy between two atoms [42]. Specifically, the hottest atom in the cold layer is exchanged with the coldest atom in the hot layer. The energy transfer is quantified by averaging over multiple such exchanges. In RNEMD, a direct temperature gradient is not applied to the system. Instead, a heat flux is introduced, and the resulting temperature gradient is calculated. This approach, where the temperature gradient is indirectly induced, leads to a more stable heat flux transfer, resulting in more convergent data [56].

At the macroscopic level, the thermal conductivity is defined according to Fourier's law as the ratio of heat flux to temperature gradient. Here, $\phi_z$ represents the thermal conductivity, $\delta$ is the heat flux, and $\nabla T$ is the temperature gradient, as shown in Eq 3:

$$\phi_z = -\delta \nabla T \tag{3}$$

Figure 2 shows the simulation box, which is divided into $N$ slices, each having the same thickness and volume, oriented perpendicular to the z-direction. Periodic boundary conditions are applied in all directions to ensure continuous heat transfer within the system. The instantaneous local dynamic temperature $T_k$ in slice $k$ is given by the Eq 4:

$$T_k = \frac{1}{3n_k k_B} \sum_{i \equiv k}^{n_k} m_i v_i^2 \tag{4}$$

where $k_B$ is the Boltzmann constant, $n_k$ is the number of atoms in the $k$-th slice, $m_i$ is the mass of the $i$-th individual atom, and $v_i$ is the velocity of the $i$-th atom.

Once the system reaches a steady state, the energy transfer due to the unphysical velocity exchange and the resulting heat flux in the reverse direction come into equilibrium. As a result, the thermal conductivity ($\lambda$) can be expressed as Eq 5:

$$\lambda = -\frac{\phi_z}{2tL_x l_y \nabla T} \tag{5}$$

where $\phi_z$ is the heat flux, 2 represents the mirror relationship of heat transfer, $t$ is the total simulation time, $L_xL_y$ is the cross-sectional area of the model perpendicular to the $z$-direction, and $\nabla T$ is the temperature gradient.

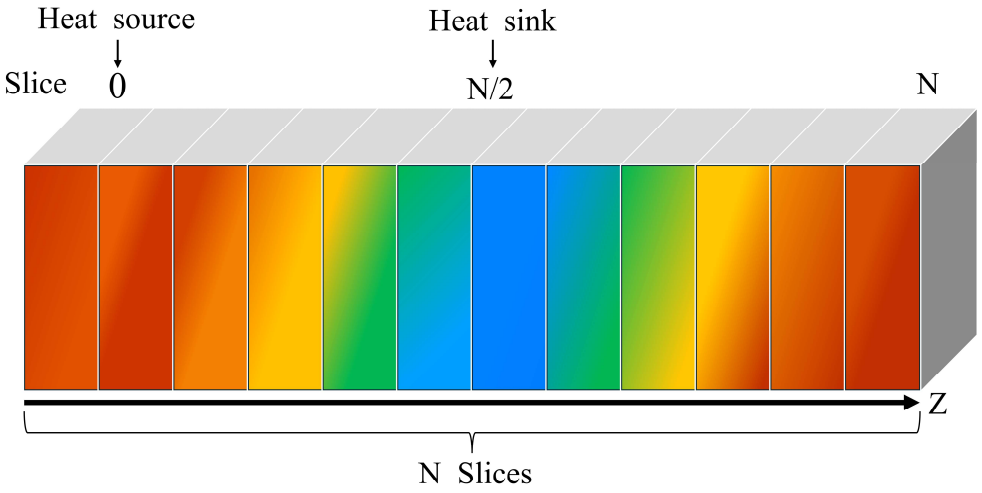


**Figure 2.** Simulation box with N slices and the resultant temperature gradient.

Slice *0* and slice *N* were defined as the "hot" layers, and slice *N/2* was defined as the "cold" layer. In the heat transfer process, the hottest atom in the cold layer exchanged kinetic energy with the coldest atom in the hot layer. These two atoms, having the same mass, underwent a velocity exchange: the velocities of the hottest atom in the cold layer and the coldest atom in the hot layer were swapped. This exchange of kinetic energy led to a redistribution of energy between the layers, causing the cold layer to lose energy and the hot layer to gain energy. As a result, a temperature difference formed between the layers, establishing a temperature gradient. Importantly, this exchange of velocities did not alter the system's total linear momentum, total kinetic energy, or total energy, as it adhered to the conservation laws. However, the total angular momentum of the system was not conserved during this process.

In this study, the geopolymer structure model was employed, and the simulation box was extended along the heat flux direction (the z-direction) with an extension ratio of at least 1:3. The system was divided into 40 slices, and simulations were performed using the UFF with a time step of 0.25 fs. Initially, the system was equilibrated at 300 K. Velocity exchanges were carried out every 100 steps (0.025 ps). During the equilibration phase in the NVT ensemble, a total of 5000 exchanges (125 ps) were performed. Afterward, the system was simulated for 10,000 exchanges (0.25 ns) under the Microcanonical Ensemble (NVE), and the thermal conductivity data was subsequently obtained.

## 3. Results and discussion

### *3.1. Energy and temperature variations of different models*

The structural properties of geopolymer materials are strongly influenced by energy and temperature fluctuations between molecules. The changes in energy and temperature, as observed from molecular dynamics simulations, provide valuable insights into the rationality and stability of the structure. Therefore, the energy and temperature variations of geopolymers with different Si/Al ratios were examined, and the results are presented in Figure 3. According to this figure, the variation curves for potential energy, total energy, and non-bonded energy exhibit similar trends, with no significant fluctuations during the simulation. This stability suggests that the system is reasonable and stable.

Notably, the total energy of the structure with a Si/Al ratio of 1 is lower than that of the other two competitors. Furthermore, the potential energy gradually increased from –26,200 at Si/Al ratio of 1 to –19,450 and –16,310 kcal/mol as the Si/Al ratio increased to 2 and 3, respectively. Similarly, the non-bonded energy increased progressively from –33,500 to –26,500 and –23,500 kcal/mol as the Si/Al ratio rose from 1 to 2 and 3, respectively.

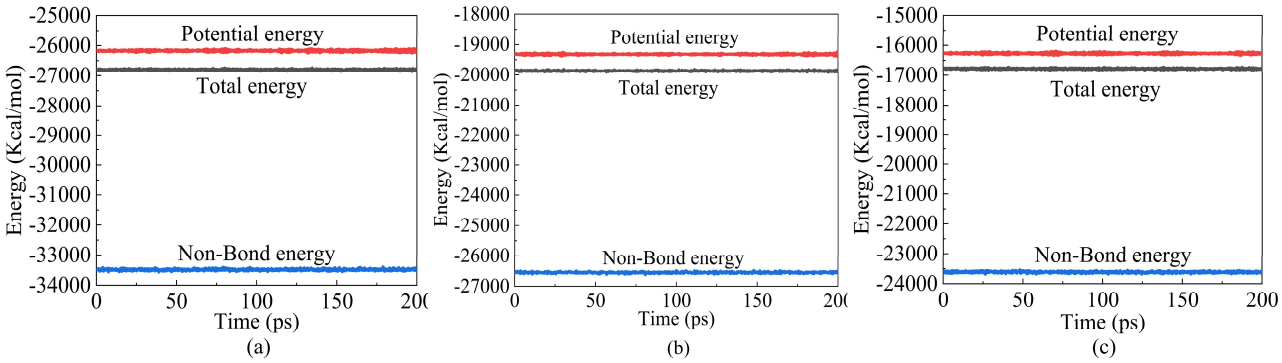


**Figure 3.** Variation of potential, total, and non-bond energy at Si/Al ratios of (a) 1, (b) 2, and (c) 3.

Figure 4 shows the temperature variation over time for systems with different Si/Al ratios. It is observed that, after 200 ps of molecular dynamics simulation at an initial temperature of 300 K, the temperature fluctuated around 300 K and remained largely stable for these three models.

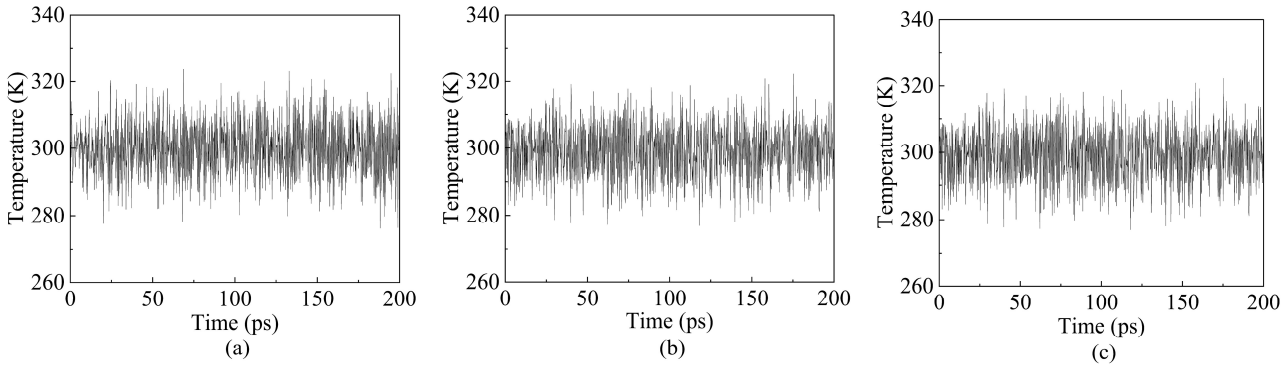


**Figure 4.** Variation of temperature with time at Si/Al ratios of (a) 1, (b) 2, and (c) 3.

In summary, all three models reached their minimum energy state after the MD simulation. Additionally, the energy of the geopolymer structure increased significantly at higher Si/Al ratios, demonstrating an improvement in structural stability.

### *3.2. Radial distribution function (RDF)*

RDF defines the probability of finding another atom within a certain distance from a given atom [57]. RDF analysis provides insights into the microscopic structural changes between different atoms in the geopolymer structure, helping to assess both the stability of the structure and the interactions between atoms. The RDF is calculated using the following Eq 6:

$$g_{(r)} = \lim_{d_r \to 0} \frac{p(r)}{4\pi\left(\frac{N_{pair}}{v}\right) r^2 \, dr} \tag{6}$$

where $v$ is the volume of the constructed model, $N_{pair}$ is the number of unique atomic pairs, $r$ is the distance between a pair of atoms, and $p(r)$ is the number of atomic pairs found within the distance range $r$ to $r + dr$.

Figure 5 shows the RDF curves for Si-Al bonds at Si/Al ratios of 1, 2, and 3 at different temperatures (300, 600, and 900 K). As expected for an amorphous structure, all curves exhibit short-range order and long-range disorder. Notable peaks appear in the short-range region (0–5 Å); beyond 5 Å, curve fluctuations gradually decrease, approaching a value of 1. This behavior is characteristic of amorphous structures and aligns well with the experimental data obtained from X-ray measurements in White's study [58].

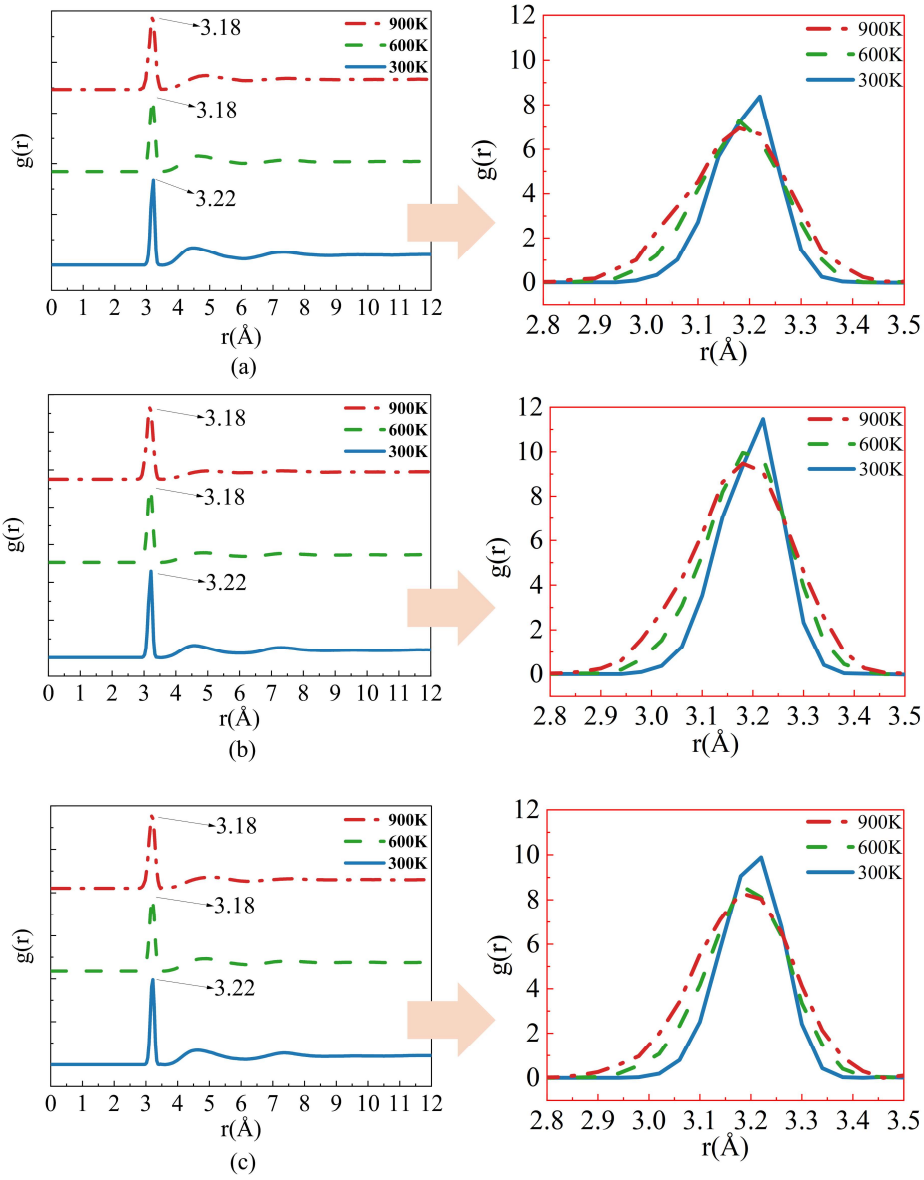


**Figure 5.** RDF of Si-Al bonds at Si/Al ratios of (a) 1, (b) 2, and (c) 3 at various temperatures.

From the RDF curves, it is observed that the peak intensity of the Si-Al bond decreased with increasing temperature, particularly within the 2.8–3.5 Å range. For all three Si/Al ratios, the peak intensity decreased more significantly between 300 and 600 K, while the reduction from 600 to 900 K was minor, with an average decrease of 0.4 Å. This trend suggests that the N-A-S-H structure becomes more stable at increased temperatures.

Additionally, for Si–Al bonds at Si/Al ratios of 1, 2, and 3, the bond length decreased from 3.22 to 3.18 Å across temperatures of 300, 600, and 900 K, with a reduction of 0.04 Å. The shortening of the Si–Al bond length increased the bond energy between atoms, indicating that the interaction between Si–Al bonds strengthens as the Si/Al ratio increases. This enhanced bond strength suggests that the geopolymer structure can maintain its high strength at elevated temperatures, further confirming its stability and heat resistance.

Furthermore, the RDFs of the Si–O and Al–O bonds were analyzed using UFF potentials, as shown in Figure 6, and the results were compared with those reported in other force field studies cited in [59]. The first RDF peak for the Si–O bond appears at 1.62 Å, which aligns well with the reported range of 1.60–1.65 Å in previous studies [60]. Similarly, the first RDF peak for the Al–O bond is located at 1.74 Å, consistent with the reported range of 1.74–1.80 Å [61]. Moreover, both the Si–O and Al–O bonds exhibit slight elongation with increasing temperature [62].

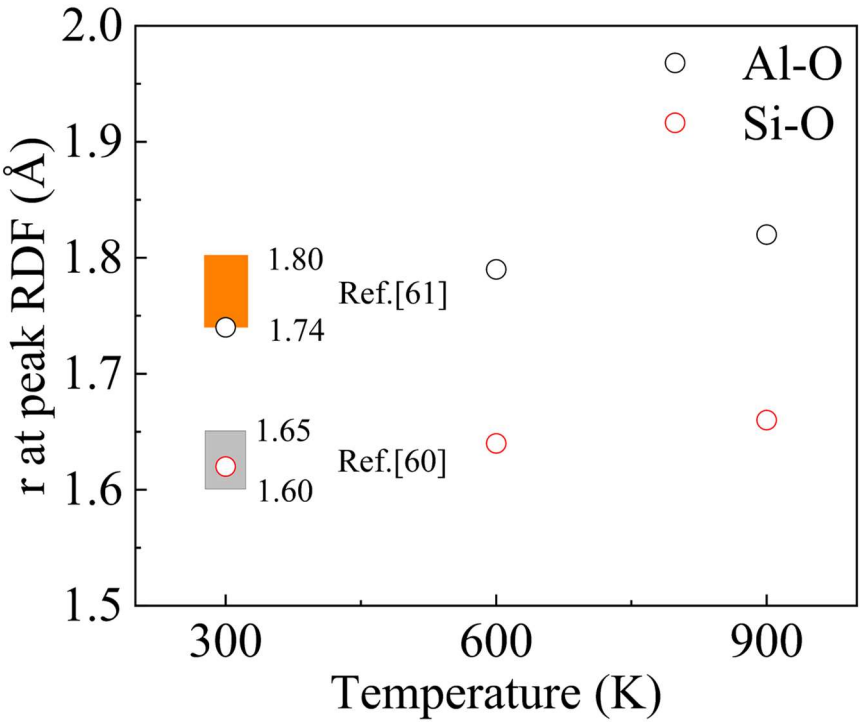


**Figure 6.** RDF of Si–O bonds and Al–O bonds at Si/Al ratios of 1 at various temperatures.

### *3.3. Mean square displacement (MSD)*

The mean square displacement (MSD) was used to quantify the diffusion extent of atoms in the geopolymer structure [54]. This is an important indicator of the molecular diffusion rate within the

system and describes the deviation of an atom's position relative to its original position. The MSD can be calculated using the Eq 7:

$$MSD = \frac{1}{N}\langle |r_i(t) - r_i(0)|^2 \rangle \quad (7)$$

where $N$ is the number of atoms, $r_i(t)$ represents the position of atom $i$ at time $t$, and is $r_i(0)$ the initial position of atom $i$ at the start of the simulation.

Figure 7 shows the MSD of Si and Al atoms over time in N-A-S-H structure with different Si/Al ratios at various temperatures (300, 600, and 900 K). The MSD values of Si and Al atoms, which form [$SiO_4$] and [$AlO_4$] tetrahedra, increased with rising temperatures. At a Si/Al ratio of 1, the MSD exhibited a more pronounced increase, with a steeper growth curve. In contrast, at higher Si/Al ratios (1.5 and 2), the growth of MSD was more gradual, showing a smoother increase over time.

At 300 K, the MSD values of Si and Al atoms were very similar for all three Si/Al ratios, showing minimal variation from 0 to 100 ps. This is due to the fact that at low temperatures, atoms absorb less energy, resulting in slower diffusion and smaller displacements, which contributes little to the thermal conductivity. In contrast, as the temperature increased to 600 and 900 K, the MSD values of Si and Al atoms increased significantly, with a larger gradient in MSD growth at 900 K. This is because, at high temperatures, atoms absorb more energy, which accelerates the vibration and diffusion of Si and Al atoms [25]. The increased diffusion would lead to higher thermal conductivity efficiency [63]. Moreover, the variations of MSD across models at different Si/Al ratios were also distinct. At 900 K, the MSD was larger at a Si/Al ratio of 1 (Figure 7a), indicating that the diffusion and vibration of Si and Al atoms were more pronounced at this ratio.

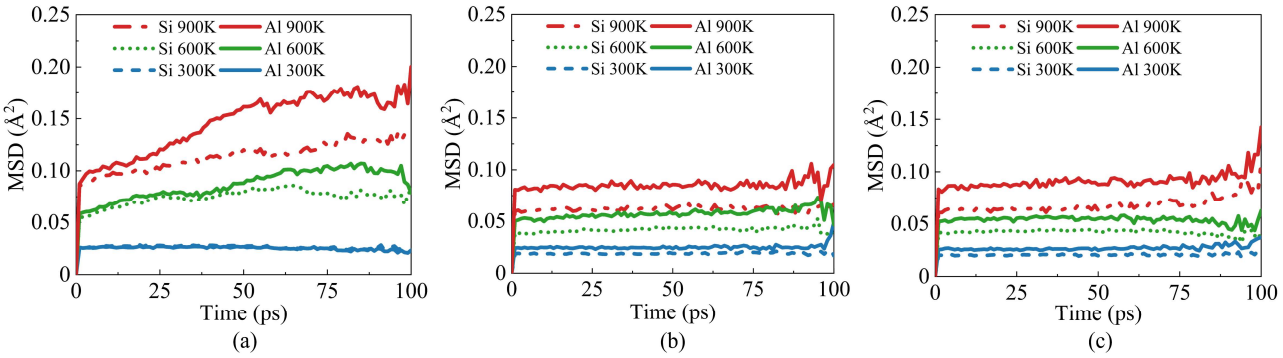


**Figure 7.** Variation of MSD with time at Si/Al ratios of (a) 1, (b) 2, and (c) 3.

Despite the clear difference in MSD across different temperatures and Si/Al ratios, the magnitudes of MSD remained within the range of 0.01–0.2 Å, which was significantly lower than those observed in previous modeling of carbon nanotubes in phase change materials [64]. This is because Si and Al atoms served as a framework of the molecular structures, and their movement was largely confined [65]. This suggests that the relatively ordered arrangement of atoms in N-A-S-H structures contributed to their higher stability [64,66].

### *3.4. Thermal conductivity analysis*

To determine the thermal conductivity of N-A-S-H models, the simulation box is extended along the heat flux direction (the z-direction in the figure), with the height-to-length ratio of 1:3, according to the requirements of the RNEMD method [42]. The reshaped simulation box is shown in Figure 8, and the quantities of the atoms were tripled.

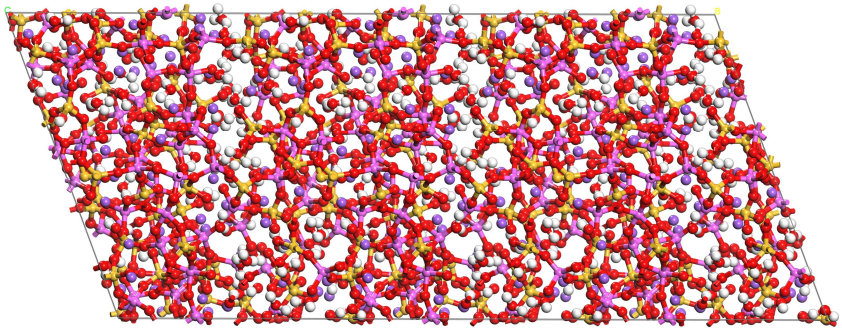

**Figure 8.** Simulation box of N-A-S-H with an extension ratio of 1:3.

Figure 9 shows the typical distributions of temperature and density along the z-direction of the simulation box at the equilibrium state, obtained at a Si/Al ratio of 1. As shown in Figure 9a, the temperature variation followed a general linear trend, indicating that the temperature gradient across the entire N-A-S-H structure remains constant, with no localized temperature fluctuations. Moreover, the heat flux that passed through the cross-sections of the simulation box was uniform and consistent. According to Fourier's law (Eq 3), this uniform temperature gradient suggested that the thermal conductivity of the geopolymer structure was uniform along the z-direction.

However, as shown in Figure 9b, the distribution of density in the simulation box fluctuated at all three temperatures. This phenomenon was also observed in previous studies [67], indicating that the convergence rate is slow, which warrants further investigation.

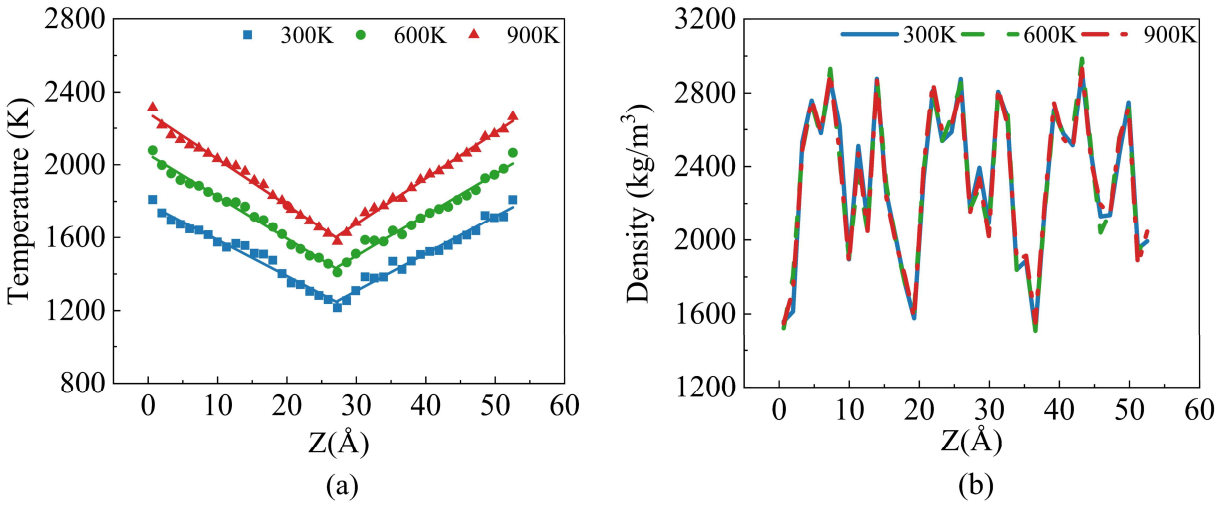


**Figure 9.** Variation of (a) temperature and (b) density along the z-direction at a Si/Al ratio of 1.

Figure 10 shows the variation of thermal conductivity over time at different temperatures and Si/Al ratios. It can be observed that thermal conductivity exhibited obvious fluctuations during the early period of the simulation. Then, the curves smoothed out and progressed linearly, indicating the convergence of the simulation. Furthermore, the simulation achieved convergence in approximately 100, 75, and 50 ps for temperatures of 300, 600, and 900 K, respectively. The shortened convergence time suggested a faster rate of steady heat transfer as temperature increases, which corresponds to the improved thermal conductivity at higher temperatures. In addition, at 600 and 900 K, the calculated thermal conductivity continued to increase after convergence was achieved. However, this does not affect the final thermal conductivity value.

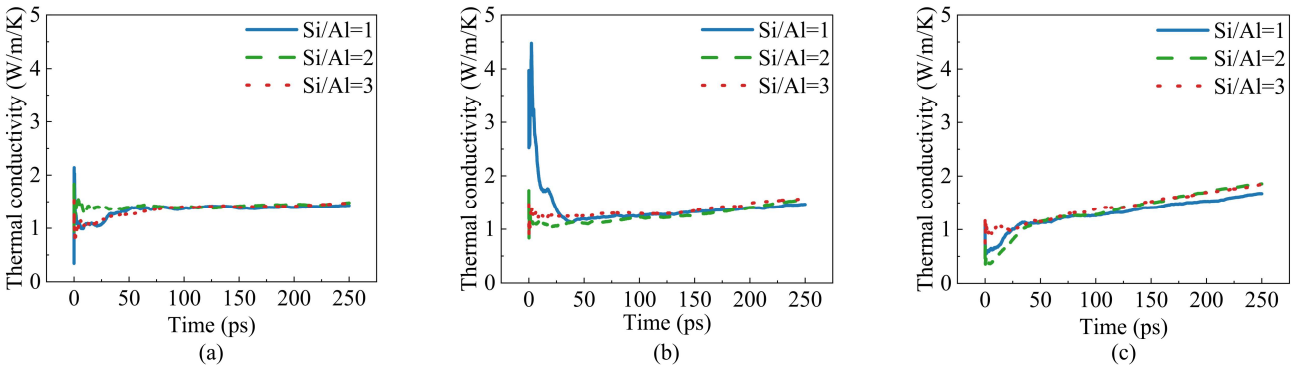


**Figure 10.** Variation of thermal conductivity with time at different temperatures: (a) 300 K, (b) 600 K, and (c) 900 K.

The final thermal conductivities of all structures at different temperatures and Si/Al ratios are shown in Figure 11. The thermal conductivities of the models changed in a range from 1.431 to 1.857 W/m/K. In addition, thermal conductivity exhibited a rising trend as the temperature increased from 300 to 600 K and increased by 2.50%, 5.88%, and 6.57% at Si/Al ratios of 1, 2, and 3, respectively. The increase became more significant from 600 to 900 K, increasing by 17.1%, 25.2%, and 25.4%, respectively, across the same Si/Al ratios.

Moreover, thermal conductivity increased substantially as the Si/Al ratio increased from 1 to 3, while most of the increase occurred as the Si/Al ratio increased from 1 to 2, exhibiting a 2.95%, 6.32%, and 10.1% increase rate at 300, 600, and 900 K, respectively. Further increases were minimal, e.g., 0.56%, 1.22%, and 0.71%, as Si/Al ratio further increased to 3. This demonstrates that N-A-S-H achieved higher thermal conductivity at higher temperatures and Si/Al ratios. The minimal variation in thermal conductivity as the Si/Al ratio increases from 2 to 3 can be attributed to the saturation of atomic interactions within the N-A-S-H structure. At higher Si/Al ratios, the additional Si atoms contribute less to the overall thermal conductivity due to the already optimized network of Si–O–Al bonds.

In addition, the variation in thermal conductivity of N-A-S-H at 300 K is compared with the observations from previous experimental studies by Kamseu et al. [21] and MD modeling by Liu et al. [20]. It can be seen that the predicted thermal conductivity of N-A-S-H is much higher than the experimental data of geopolymer concrete. This discrepancy arises because N-A-S-H is only one component of geopolymer concrete, which also includes coarse and fine aggregates as well as other crystal phases within the geopolymer gel. Nevertheless, the overall trends in thermal conductivity

variations are consistent, highlighting the influence of N-A-S-H components on the properties of the geopolymer concrete and validating the accuracy of the predicted results.

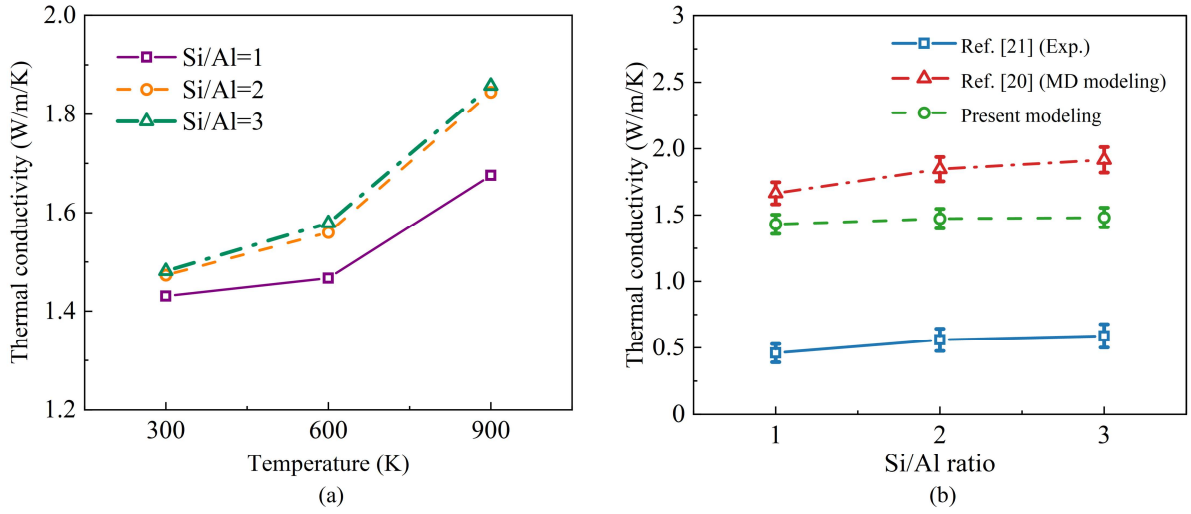


**Figure 11.** Variation of thermal conductivity at (a) different temperatures and (b) Si/Al ratios.

## 4. Conclusions

This study simulates the molecular structural variation of hydrated sodium aluminosilicate (N-A-S-H) gel exposed to extremely elevated temperatures. The effects of Si/Al ratios and temperature levels on the molecular structural characteristics and atomic mobility were analyzed using the radial distribution function (RDF) and mean square displacement (MSD), while the thermal conductivity was predicted using the reverse nonequilibrium molecular dynamics (RNEMD) method. Based on the results and discussion, the following conclusions can be drawn:

1. The potential energy and non-bonding energy of the system with a Si/Al ratio of 1 were the lowest, and the system remained in equilibrium throughout the simulation. As the Si/Al ratio increased, the system's energy gradually increased, and its structural stability improved.

2. The Si-Al bond length in N-A-S-H decreased as the temperature increased, indicating that the geopolymer structure exhibits good stability at high temperatures.

3. The root mean square displacement (MSD) of Si and Al atoms increased with rising temperatures, suggesting that atomic vibrations and diffusion become more pronounced as temperature increases.

4. The thermal conductivity of N-A-S-H ranged from 1.431 to 1.857 W/m/K at Si/Al ratios of 1 to 3 and temperatures from 300 to 900 K.

5. Thermal conductivity of N-A-S-H increased as temperature increased from 300 to 900 K. A more pronounced increase occurred as temperature increased from 600 to 900 K, exhibiting 17.1%, 25.2%, and 25.4% increased ratios at Si/Al ratios of 1, 2, and 3, respectively.

6. The thermal conductivity of N-A-S-H increased by 2.95%, 6.32%, and 10.1%, at 300, 600, and 900 K, respectively, as the Si/Al ratio increased from 1 to 2, while remaining almost invariant as Si/Al further increased to 3.

7. This study reveals the intrinsic mechanism of the change of N-A-S-H gel properties under high-temperature conditions through different Si/Al ratios and temperatures, providing a theoretical

basis for the development of new low-carbon, environmentally friendly, and high-temperature-resistant building materials, and offering strong support for the evaluation of long-term durability and safety of materials in engineering practices.

## Use of AI tools declaration

The authors declare they have not used Artificial Intelligence (AI) tools in the creation of this article.

## Acknowledgments

This study was supported by the National Natural Science Foundation of China (Nos. 52408323 and 52178278), the Anhui Provincial Universities Natural Science Research Project (Nos. KJ2020ZD43 and 2022AH050261), the Anhui Provincial Natural Science Foundation Project (No. 1908085ME144), the Anhui Province Housing and Urban-Rural Development Science and Technology Program (No. 2023-YF133), and the Doctoral Startup Foundation from Anhui Jianzhu University (No. 2022QDZ23). Additional support was provided by the Department of Science and Technology of Guangdong Province, China (Nos. 2023A1515110842 and 2023A1515110542), the Open Foundation of the Key Lab of Prefabricated Building Research Institute of Anhui Province (No. AHZPY2023KF02), Anhui Jianzhu University Ph.D. Foundation (No. 2019QDZ29), and the University Synergy Innovation Program of Anhui Province (No. GXXT-2023-061). Special thanks also go to the National-Local Joint Engineering Laboratory of Building Health Monitoring and Disaster Prevention Technology (Grant No. GG23KF006).

## Author contributions

Liu Yun-Lin: conceptualization, supervision; Ren Si-Yu: writing—original draft, methodology, data curation; Wang Dong-Hua: supervision; Yang Ding-Wei: project administration; Kai Ming-Feng: methodology; Guo Dong: investigation, writing-review & editing; validation.

## Conflict of interest

The authors declare no conflict of interest.

## References

1. Hayat U, Kai MF, A HB, et al. (2024) Atomic-level investigation into the transport of NaCl solution in porous cement paste: The effects of pore size and temperature. *J Build Eng* 86: 108976. https://doi.org/10.1016/j.jobe.2024.108976
2. Liu YL, Li CF, Zhai HX, et al. (2023) Production and performance of $CO_2$ modified foam concrete. *Constr Build Mater* 389: 131671. https://doi.org/10.1016/j.conbuildmat.2023.131671
3. Maddalena R, Roberts JJ, Hamilton A, et al. (2018) Can Portland cement be replaced by low-carbon alternative materials? A study on the thermal properties and carbon emissions of innovative cements. *J Clean Prod* 186: 933–942. https://doi.org/10.1016/j.jclepro.2018.02.138

4. Chairunnisa N, Haryanti NH, Nurwidayati R, et al. (2024) Characteristics of metakaolin-based geopolymers using bemban fiber additives. *AIMS Mater Sci* 11: 815–832. https://doi.org/10.3934/matersci.2024040
5. Liu Y, Huo S, Fu J, et al. (2024) Dynamic properties of $CO_2$-cured foam concrete at different loading rates: Effect of the foam admixtures and addition of polypropylene fiber. *Front Mater* 11: 1445848. https://doi.org/10.3389/fmats.2024.1445848
6. Hassan A, Arif M, Shariq M, et al. (2022) Fire resistance characteristics of geopolymer concrete for environmental sustainability: A review of thermal, mechanical and microstructure properties. *Environ Dev Sustain* 25: 8975–9010. https://doi.org/10.1007/s10668-022-02495-0
7. He R, Dai N, Wang Z, et al. (2020) Thermal and mechanical properties of geopolymers exposed to high temperature: A literature review. *Adv Civ Eng* 2020: 7532703. https://doi.org/10.1155/2020/7532703
8. Habert G, De Lacaillerie JB, Roussel N, et al. (2011) An environmental evaluation of geopolymer based concrete production: Reviewing current research trends. *J Clean Prod* 19: 1229–1238. https://doi.org/10.1016/j.jclepro.2011.03.012
9. Mahmoud HA, Tawfik TA, Abd El-razik MM, et al. (2023) Mechanical and acoustic absorption properties of lightweight fly ash/slag-based geopolymer concrete with various aggregates. *Ceram Int* 49: 21142–21154. https://doi.org/10.1016/j.ceramint.2023.03.244
10. Mathew G, Issac BM (2020) Effect of molarity of sodium hydroxide on the aluminosilicate content in laterite aggregate of laterised geopolymer concrete. *J Build Eng* 32: 101486. https://doi.org/10.1016/j.jobe.2020.101486
11. Liu YL, Liu C, Qian LP, et al. (2023) Foaming processes and properties of geopolymer foam concrete: Effect of the activator. *Constr Build Mater* 391: 131830. https://doi.org/10.1016/j.conbuildmat.2023.131830
12. Duxson P, Fernández-Jiménez A, Provis JL, et al. (2006) Geopolymer technology: The current state of the art. *J Mater Sci* 42: 2917–2933. http://dx.doi.org/10.1007/s10853-006-0637-z
13. Li W, Wang Y, Yu C, et al. (2022) Nano-scale study on molecular structure, thermal stability, and mechanical properties of geopolymer. *J Korean Ceram Soc* 60: 413–423. https://doi.org/10.1007/s43207-022-00276-z
14. Shang J, Dai JG, Zhao TJ, et al. (2018) Alternation of traditional cement mortars using fly ash-based geopolymer mortars modified by slag. *J Clean Prod* 203: 746–756. https://doi.org/10.1016/j.jclepro.2018.08.255
15. Lemougna PN, Adediran A, Yliniemi J, et al. (2020) Thermal stability of one-part metakaolin geopolymer composites containing high volume of spodumene tailings and glass wool. *Cem Concr Compos* 114: 103792. https://doi.org/10.1016/j.cemconcomp.2020.103792
16. Cheng TW, Chiu JP (2003) Fire-resistant geopolymer produced by granulated blast furnace slag. *Miner Eng* 16: 205–210. https://doi.org/10.1016/S0892-6875(03)00008-6
17. Amran M, Huang SS, Debbarma S, et al. (2022) Fire resistance of geopolymer concrete: A critical review.*Constr Build Mater* 324: 126722. https://doi.org/10.1016/j.conbuildmat.2022.126722
18. Temuujin J, Minjigmaa A, Rickard W, et al. (2010) Fly ash based geopolymer thin coatings on metal substrates and its thermal evaluation. *J Hazard Mater* 180: 748–752. https://doi.org/10.1016/j.jhazmat.2010.04.121
19. Abdolhosseini Qomi MJ, Ulm FJ, Pellenq RJM (2015) Physical origins of thermal properties of cement paste. *Phys Rev Appl* 3: 064010. https://doi.org/10.1103/PhysRevApplied.3.064010

20. Liu W, Ju S (2024) Tunable thermal conductivity of sustainable geopolymers by the Si/Al ratio and moisture content: Insights from atomistic simulations. *J Phys Chem B* 128: 2972–2984. https://doi.org/10.1021/acs.jpcb.3c07445
21. Kamseu E, Ceron B, Tobias H, et al. (2011) Insulating behavior of metakaolin-based geopolymer materials assess with heat flux meter and laser flash techniques. *J Therm Anal Calorim* 108: 1189–1199. https://doi.org/10.1007/s10973-011-1798-9
22. Akbulut ZF, Guler S, Khan M, et al. (2023) The effects of waste iron powder and steel fiber on the physical and mechanical properties of geopolymer mortars exposed to high temperatures. *Structures* 58: 105398. https://doi.org/10.1016/j.istruc.2023.105398
23. Samal S, Phan Thanh N, Petríková I, et al. (2015) Improved mechanical properties of various fabric-reinforced geocomposite at elevated temperature. *JOM* 67: 1478–1485. https://doi.org/10.1007/s11837-015-1420-x
24. Wang J, Chen X, Li C, et al. (2023) Evaluating the effect of kaliophilite on the fire resistance of geopolymer concrete. *J Build Eng* 75: 106975. https://doi.org/10.1016/j.jobe.2023.106975
25. Kupwade-Patil K, Soto F, Kunjumon A, et al. (2013) Multi-scale modeling and experimental investigations of geopolymeric gels at elevated temperatures. *Comput Struct* 122: 164–177. https://doi.org/10.1016/j.compstruc.2013.01.005
26. Kong DL, Sanjayan JG, Sagoe-Crentsil K, et al. (2007) Factors affecting the performance of metakaolin geopolymers exposed to elevated temperatures. *J Mater Sci* 43: 824–831. https://doi.org/10.1007/s10853-007-2205-6
27. Cai J, Li X, Tan J, et al. (2020) Thermal and compressive behaviors of fly ash and metakaolin-based geopolymer. *J Build Eng* 30: 101307. https://doi.org/10.1016/j.jobe.2020.101307
28. Agustini NKA, Triwiyono A, Sulistyo D, et al. (2020) Effects of water to solid ratio on thermal conductivity of fly ash-based geopolymer paste. *IOP Conf Ser Earth Environ Sci* 426: 012010. https://doi.org/10.1088/1755-1315/426/1/012010
29. Pan Z, Tao Z, Cao YF, et al. (2018) Compressive strength and microstructure of alkali-activated fly ash/slag binders at high temperature. *Cem Concr Compos* 86: 9–18. https://doi.org/10.1016/j.cemconcomp.2017.09.011
30. Wang P, Zhang Q, Wang M, et al. (2019) Atomistic insights into cesium chloride solution transport through the ultra-confined calcium–silicate–hydrate channel. *Phys Chem Chem Phys* 21: 11892–11902. https://doi.org/10.1039/C8CP07676F
31. Chen Y, de Lima LM, Li Z, et al. (2024). Synthesis, solubility and thermodynamic prperties of NASH gels with various target Si/Al ratios. *Cem Concr Res* 180: 107484. https://doi.org/10.1016/j.cemconres.2024.107484
32. Zhang W, Lang L, Chen X, et al. (2024) Adsorption mechanism of $C_s^+$ and $Pb_2^+$ on the NASH surface under the different Si/Al ratio and temperature. *J Mol Liq* 40: 124558. https://doi.org/10.1016/j.molliq.2024.124558
33. He Y, Savic I, Donadio D, et al. (2012) Lattice thermal conductivity of semiconducting bulk materials: Atomistic simulations. *Phys Chem Chem Phys* 14: 16209–16222. https://doi.org/10.1039/C2CP42394D
34. Yousefi F, Khoeini F, Rajabpour A, et al. (2020) Thermal conductivity and thermal rectification of nanoporous graphene: A molecular dynamics simulation. *Int J Heat Mass Transf* 146: 118884. https://doi.org/10.1016/j.ijheatmasstransfer.2019.118884

35. Zhang X, Xie H, Hu M, et al. (2014) Thermal conductivity of silicene calculated using an optimized Stillinger-Weber potential. *Phys Rev B* 89: 054310. https://doi.org/10.1103/PhysRevB.89.054310
36. Zhang X, Zhang J, Yang M, et al. (2020) Molecular dynamics study on the thermal conductivity of bilayer graphene with nitrogen doping. *Solid State Commun* 309: 113845. https://doi.org/10.1016/j.ssc.2020.113845
37. Che J, Çağın T, Deng W, et al. (2000) Thermal conductivity of diamond and related materials from molecular dynamics simulations. *J Chem Phys* 113: 6888–6900. https://doi.org/10.1063/1.1310223
38. Jund P, Jullien R (1999) Molecular-dynamics calculation of the thermal conductivity of vitreous silica. *Phys Rev B* 59: 13707–13711. https://doi.org/10.1103/PhysRevB.59.13707
39. Tretiakov KV, Scandolo S (2004) Thermal conductivity of solid argon at high pressure and high temperature: A molecular dynamics study. *J Chem Phys* 121: 11177–11182. https://doi.org/10.1063/1.1812754
40. Esfarjani K, Chen G, Stokes HT, et al. (2011) Heat transport in silicon from first-principles calculations. *Phys Rev B* 84: 085204. https://doi.org/10.1103/PhysRevB.84.085204
41. Schelling PK, Phillpot SR, Keblinski P, et al. (2002) Comparison of atomic-level simulation methods for computing thermal conductivity. *Phys Rev B* 65: 144306. https://doi.org/10.1103/PhysRevB.65.144306
42. Müller-Plathe F (1997) A simple nonequilibrium molecular dynamics method for calculating the thermal conductivity. *J Chem Phys* 106: 6082–6085. https://doi.org/10.1063/1.473271
43. Du H, Shi J, Chen Z, et al. (2022) Reverse nonequilibrium molecular dynamics simulation for thermal conductivity of gallium-based liquid metal. *J Phys Chem C* 126: 20558–20569. https://doi.org/10.1021/acs.jpcc.2c04023
44. Loulijat H, Moustabchir H (2021) A study of the effects of graphene nanosheets on the thermal conductivity of nanofluid (argon-graphene) using reverse nonequilibrium molecular dynamics method. *Int J Thermophys* 42: 125. https://doi.org/10.1007/s10765-021-02877-y
45. Zhu M, Li J, Chen J, et al. (2019) Improving thermal conductivity of epoxy resin by filling boron nitride nanomaterials: A molecular dynamics investigation. *Comput Mater Sci* 164: 108–115. https://doi.org/10.1016/j.commatsci.2019.04.012
46. Zhang C, Hao XL, Wang CX, et al. (2017) Thermal conductivity of graphene nanoribbons under shear deformation: A molecular dynamics simulation. *Sci Rep* 7: 41398. https://doi.org/10.1038/srep41398
47. Shabib I, Abu-Shams M, Khan MR, et al. (2014) Lattice thermal conductivity of Fe-Cr alloys with <001> tilt boundaries: An atomistic study. Proceedings of the ASME 2014 International Mechanical Engineering Congress and Exposition. Volume 9: Mechanics of Solids, Structures and Fluids. Montreal, Quebec, Canada. https://doi.org/10.1115/IMECE2014-38408
48. Wan H, Yuan L, Zhang Y, et al. (2020) Insight into the leaching of sodium alumino-silicate hydrate (N-A-S-H) gel: A molecular dynamics study. *Front Mater* 7: 56. https://doi.org/10.3389/fmats.2020.00056
49. Tian Z, Zhang Z, Tang X, et al. (2023) Understanding the effect of moisture on interfacial behaviors of geopolymer-aggregate interaction at molecular level. *Constr Build Mater* 385: 131404. https://doi.org/10.1016/j.conbuildmat.2023.131404

50. Wang R, Wang J, Dong T, et al. (2020) Structural and mechanical properties of geopolymers made of aluminosilicate powder with different $SiO_2/Al_2O_3$ ratio: Molecular dynamics simulation and microstructural experimental study. *Constr Build Mater* 240: 117935. https://doi.org/10.1016/j.conbuildmat.2019.117935
51. Wang R, Wang J, Song Q, et al. (2021) The effect of $Na^+$ and $H_2O$ on structural and mechanical properties of coal gangue-based geopolymer: Molecular dynamics simulation and experimental study. *Constr Build Mater* 268: 121081. https://doi.org/10.1016/j.conbuildmat.2020.121081
52. Bagheri A, Nazari A, Sanjayan JG, et al. (2018) Molecular simulation of water and chloride ion diffusion in nanopores of alkali-activated aluminosilicate structures. *Ceram Int* 44: 20723–20731. https://doi.org/10.1016/j.ceramint.2018.08.067
53. Bagheri A, Nazari A, Sanjayan JG, et al. (2017) Fly ash-based boroaluminosilicate geopolymers: Experimental and molecular simulations. *Ceram Int* 43: 4119–4126. https://doi.org/10.1016/j.ceramint.2016.12.020
54. Chitsaz S, Tarighat A (2020) Molecular dynamics simulation of N-A-S-H geopolymer macro molecule model for prediction of its modulus of elasticity. *Constr Build Mater* 243: 118176. https://doi.org/10.1016/j.conbuildmat.2020.118176
55. Hou D, Zhang Y, Yang T, et al. (2018). Molecular structure, dynamics, and mechanical behavior of sodium aluminosilicate hydrate (NASH) gel at elevated temperature: A molecular dynamics study. *Phys Chem Chem Phys* 20: 20695–20711. https://doi.org/10.1039/C8CP03411G
56. Mahajan SS, Subbarayan G, Sammakia BG, et al. (2007) Estimating thermal conductivity of amorphous silica nanoparticles and nanowires using molecular dynamics simulations. *Phys Rev E* 76: 056701. https://doi.org/10.1103/PhysRevE.76.056701
57. Kai MF, Zhang LW, Liew KM, et al. (2019) Graphene and graphene oxide in calcium silicate hydrates: Chemical reactions, mechanical behavior and interfacial sliding. *Carbon* 146: 181–193. https://doi.org/10.1016/j.carbon.2019.01.097
58. White CE, Page K, Henson NJ, et al. (2013) In situ synchrotron X-ray pair distribution function analysis of the early stages of gel formation in metakaolin-based geopolymers. *Appl Clay Sci* 73: 17–25. https://doi.org/10.1016/j.clay.2012.09.009
59. Xu LY, Alrefaei Y, Wang YS, et al. (2021) Recent advances in molecular dynamics simulation of the NASH geopolymer system: Modeling, structural analysis, and dynamics. *Constr Build Mater* 276: 122196. https://doi.org/10.1016/j.conbuildmat.2020.122196
60. Meral C, Benmore CJ, Monteiro PJM, et al. (2011) The study of disorder and nanocrystallinity in C–S–H, supplementary cementitious materials and geopolymers using pair distribution function analysis. *Cem Concr Res* 41: 696–710. https://doi.org/10.1016/j.cemconres.2011.03.027
61. White CE, Provis JL, Proffen T, et al. (2010) The effects of temperature on the local structure of metakaolin-based geopolymer binder: A neutron pair distribution function investigation. *J Am Ceram Soc* 93: 3486–3492. https://doi.org/10.1111/j.1551-2916.2010.03906.x
62. Hou D, Zhang J, Pan W, et al. (2020) Nanoscale mechanism of ions immobilized by the geopolymer: A molecular dynamics study. *J Nucl Mater* 528: 151841. https://doi.org/10.1016/j.jnucmat.2019.151841
63. Tafrishi H, Sadeghzadeh S, Ahmadi R, et al. (2020) Investigation of tetracosane thermal transport in presence of graphene and carbon nanotube fillers—A molecular dynamics study. *J Energy Storage* 29: 101321. https://doi.org/10.1016/j.est.2020.101321

64. Du Y, Zhou T, Zhao C, et al. (2022) Molecular dynamics simulation on thermal enhancement for carbon nano tubes (CNTs) based phase change materials (PCMs). *Int J Heat Mass Transfer* 182: 122017. https://doi.org/10.1016/j.ijheatmasstransfer.2021.122017
65. Guan X, Jiang L, Fan D, et al. (2022) Molecular simulations of the structure-property relationships of N-A-S-H gels. *Constr Build Mater* 329: 127166. https://doi.org/10.1016/j.conbuildmat.2022.127166
66. Qian X, Zhou J, Chen G, et al. (2021) Phonon-engineered extreme thermal conductivity materials. *Nat Mater* 20: 1188–1202. https://doi.org/10.1038/s41563-021-00918-3
67. Zhang M, Lussetti E, Muller-Plathe F, et al. (2005) Thermal conductivities of molecular liquids by reverse nonequilibrium molecular dynamics. *J Phys Chem B* 109: 15060–15067. https://doi.org/10.1021/jp0512255


AIMS Press